Available online at www.sciencedirect.com
SCIENCE DIRECT®
Optics Communications 223 (2003) 123–135
OPTICS COMMUNICATIONS
www.elsevier.com/locate/optcom

Degenerate intracavity parametric processes with injected signal

M.K. Olsen [a,*], K. Dechoum [a], L.I. Plimak [b]

[a] *Instituto de Física da Universidade Federal Fluminense, Boa Viagem 24210-340, Niterói, Rio de Janeiro, Brazil*
[b] *Fachbereich Physik, Universität Kaiserslautern, 67663 Kaiserslautern, Germany*

Received 19 February 2003; received in revised form 13 May 2003; accepted 12 June 2003

Abstract

A common way of increasing the efficiency of optical frequency conversion processes is by the injection of a coherent signal at the desired frequency. We study the efficiency of this method and its effect on the quantum statistics of the fields by performing theoretical analyses of the intracavity parametric $\chi^{(2)}$ processes of second harmonic generation and degenerate optical parametric oscillation with injected signal fields. We find that the threshold behaviour of the optical parametric oscillator with an injected signal field gives further insight into the normal threshold behaviour, considered as a limiting case as the signal field goes to zero. An injected signal is also shown to change the critical points of the systems, which define the region where the maximum of noise suppression and other quantum effects may be expected. We also investigate the self-pulsing behaviour of second harmonic generation, showing how an injected signal can affect the oscillations. We show the process of second harmonic generation can be blocked by an injected signal of the appropriate intensity, effectively removing the crystal from the cavity.

PACS: 42.50.Ct; 42.65.Ky; 42.50.Dv; 42.50.Lc

Keywords: Quantum optics; Quantum correlations; Fully quantum analysis; Parametric processes

1. Introduction

Intracavity second harmonic generation (SHG) and parametric downconversion are relatively simple non-linear optical processes which can exhibit non-classical behaviour and allow for experimental tests of quantum mechanics. Intracavity downconversion of a pump field, otherwise known as the optical parametric oscillator (OPO), has been shown to exhibit a wealth of non-classical behaviour, much of which has been described in a recent review article [1] and in the references contained therein. As the amount of work published on this topic is enormous, we will mention mainly some of the more recent publications here, beginning with Andrews et al. [2], which uses a microscopic theory, including dispersion within the

* Corresponding author. Tel.: +5521-2620-6735; fax: +5521-2620-3881.
E-mail address: mko@if.uff.br (M.K. Olsen).

0030-4018/03/$ - see front matter © 2003 Published by Elsevier Science B.V.
doi:10.1016/S0030-4018(03)01645-6

cavity, that reproduces some below threshold experimental results of Lu and Ou [3], including the width of the single-mode correlation function and the cavity enhancement factor. A theoretical investigation of the effects of quantum noise on pattern formation in the degenerate OPO [4] shows that quantum effects are important in the sustaining of patterns in a regime where a linearised analysis is expected to break down. The changes in behaviour for an unstable cavity with non-orthogonal modes have been investigated, showing that the threshold behaviour can be affected by the excess noise inherent in such a system [5]. Noise reduction in both quadrature and intensity in an OPO with a triply resonant cavity has also been measured [6]. Noise reduction in the intensity difference of the output intensities in both the degenerate and non-degenerate cases have been calculated and measured for input powers up to 14 times the threshold value [7].

Intracavity second harmonic generation can provide a relatively simple source of amplitude squeezed and sub-Poissonian light [8]. The quantum properties of the fields have been predicted to play an important role in pattern formation [9]. The competing $\chi^{(2)}$ processes of up and down-conversion within the same cavity have been theoretically and experimentally investigated, finding that many of the properties are changed when both are present [10–12]. The presence of a $\chi^{(3)}$ component, inherent to all materials, can change the properties of the fields produced by the process of second harmonic generation [13], as can detuning of the cavity [14]. What we demonstrate in this paper is that the influence of an injected signal can also change the behaviour of the intracavity fields, in both the mean field intensities and in the quantum statistics, sometimes in a counterintuitive fashion.

With an injected signal, we find that a classical analysis gives some physical insight into the well known near-threshold behaviour of the optical parametric oscillator (OPO), showing how this behaviour can be changed markedly by injection of a signal field, which acts to stimulate the production of the low-frequency mode within the cavity. This system has previously been analysed as a noiseless amplifier [15], with the statistical properties being calculated via a linearised fluctuation analysis, even though this is not expected to reproduce accurately the noise properties near any critical operating points [16]. Here, we go further, using a fully quantum analyses with the positive-P representation [17] in regions where linearisation is not valid. Even though the equations for the positive-P representation variables must generally be solved numerically, they are expected to give correct predictions for any operator moments, as long as the stochastic integration converges. In this way we are able to investigate the effects of the injected signal on both the mean fields and the quantum statistics, showing that in some cases a small change in the inputs can have a noticeably greater effect on the outputs. This is shown to be the case for the injected OPO, and for sub/second harmonic generation near the boundaries of different operating regions.

2. System and equations of motion

The degenerate parametric oscillator and intracavity second harmonic generation both consist of a non-linear $\chi^{(2)}$ medium (generally a crystal), placed inside an optical resonator. The resonator is pumped at a certain frequency and produces light at either half or twice this frequency, due to the second order non-linear susceptibility of the crystal. When the cavity is pumped at both frequencies, which process will dominate depends on the relative strengths of the two inputs. The general system can be described by the following Hamiltonian,

$$H = H_{\text{free}} + H_{\text{int}} + H_{\text{pump}} + H_{\text{damp}}, \tag{1}$$

where

$$\begin{aligned} H_{\text{free}} &= \hbar\omega_a \hat{a}^\dagger \hat{a} + \hbar\omega_b \hat{b}^\dagger \hat{b}, \\ H_{\text{int}} &= \mathrm{i}\hbar \frac{\kappa}{2}\left[\hat{a}^{\dagger\,2}\hat{b} - \hat{a}^2 \hat{b}^\dagger\right], \\ H_{\text{pump}} &= \mathrm{i}\hbar\left[\epsilon_a \hat{a}^\dagger - \epsilon_a^* \hat{a} + \epsilon_b \hat{b}^\dagger - \epsilon_b^* \hat{b}\right], \\ H_{\text{damp}} &= \hat{a}\Gamma_a^\dagger + \hat{a}^\dagger \Gamma_a + \hat{b}\Gamma_b^\dagger + \hat{b}^\dagger \Gamma_b. \end{aligned} \tag{2}$$

In the above, $\hat{a}$ and $\hat{b}$ are the annihilation operators for the intracavity modes at frequencies ω_a and ω_b, respectively, with $\omega_b = 2\omega_a$, the ϵ_j are the classical

pumping rates at each frequency and κ represents the effective non-linearity of the medium. The Γ_j are bath operators for each mode and we will assume that the bath is at zero temperature, which is a very good approximation for optical systems.

There are now several options available for the analysis of this system, starting with the Heisenberg equations of motion for the field operators, which would give a complete quantum description, but unfortunately, being non-linear coupled operator equations, are insoluble for realistic parameters. As we wish to perform a fully quantum analysis, especially in the regions where standard linearisation procedures are not valid, we will use the positive-P representation [17]. This representation allows for a statistically complete representation of the density matrix of the system, the equations of motion for the positive-P variables allowing for the stochastic calculation of any operator moment which can be written in time-normal order. Proceeding in the usual way via the master and Fokker–Planck equations for the system [18], and making the correspondence between the operators $\hat{a}$, $\hat{a}^\dagger$, $\hat{b}$, $\hat{b}^\dagger$ and the c-number variables α, α^+, β, β^+, we find the set of Itô stochastic differential equations in the positive-P representation [17,19],

$$\begin{aligned}
\frac{\mathrm{d}\alpha}{\mathrm{d}t} &= \epsilon_a - \gamma_a\alpha + \kappa\alpha^+\beta + \sqrt{\kappa\beta}\eta_1(t),\\
\frac{\mathrm{d}\alpha^+}{\mathrm{d}t} &= \epsilon_a^* - \gamma_a\alpha^+ + \kappa\alpha\beta^+ + \sqrt{\kappa\beta^+}\eta_2(t),\\
\frac{\mathrm{d}\beta}{\mathrm{d}t} &= \epsilon_b - \gamma_b\beta - \frac{\kappa}{2}\alpha^2,\\
\frac{\mathrm{d}\beta^+}{\mathrm{d}t} &= \epsilon_b^* - \gamma_b\beta^+ - \frac{\kappa}{2}\alpha^{+^2}.
\end{aligned} \tag{3}$$

In the above equations, the pairs α, α^+ and β, β^+ represent the intracavity fields at frequencies ω_a and ω_b and the γ_j are the cavity losses at each frequency. Note that, as always in the positive-P representation, the variables with crosses are not complex conjugate to the uncrossed variables except in the mean, due to the independence of the noise sources, which have the correlations

$$\overline{\eta_j} = 0,\ \overline{\eta_j(t)\eta_k(t')} = \delta_{jk}\delta(t-t'). \tag{4}$$

In the case of $\epsilon_a = 0$ we find the standard equations for the degenerate parametric oscillator, while $\epsilon_b = 0$ gives the standard equations for second harmonic generation. Although the above equations can only be solved numerically, by averaging over a large number of trajectories, the solutions to any desired operator moment can be found as, for example,

$$\lim_{N\to\infty}\frac{1}{N}\overline{\alpha^{+\,m}(t')\alpha^n(t)} = \langle :\hat{a}^{\dagger\,m}(t')\hat{a}^n(t):\rangle, \tag{5}$$

where $:\ldots:$ signifies time-normal order. In this sense the positive-P representation gives a full-quantum description of the system, albeit probabilistically. In practice we do not, of course, use an infinite number of trajectories, but use a sufficiently large number to ensure good convergence of the solutions.

In what follows, we will use three different analyses. By removing the noise terms from the positive-P equations, we are able to find the classical steady-state solutions for the fields. These solutions can then be used in a semi-classical linearised fluctuation analysis, in the operating regimes where this can be shown to be valid. We will now investigate some aspects of these solutions, and, where they are not reliable, give full quantum solutions derived from stochastic integration of the positive-P equations.

3. Injected parametric oscillator

3.1. Classical behaviour

In this section we are interested in cases where the pump is much more intense than the injected signal, i.e., $\epsilon_b \gg \epsilon_a$, while in Section 4 we will examine cases where $\epsilon_a \gg \epsilon_b$ and cases where the two pump intensities are of the same order of magnitude. Steady state classical solutions for this system have previously been given by Protsenko et al. [15], who used these as the basis for a linearised fluctuation analysis. We follow a less general approach here, considering only the case of a doubly resonant cavity with real pumping (i.e., both pump and signal have the same phase), in order to emphasise the effect of the injected signal on the threshold behaviour. Setting the noise terms to zero in Eq. (3) gives two coupled classical equations for the mean field solutions of the system,

$$\frac{d\alpha}{dt} = \epsilon_a - \gamma_a\alpha + \kappa\alpha^*\beta,$$
$$\frac{d\beta}{dt} = \epsilon_b - \gamma_b\beta - \frac{\kappa}{2}\alpha^2. \quad (6)$$

Setting the left-hand sides to zero, and considering that on resonance the two field amplitudes are real for the in-phase solutions [20], gives the following solution for α_{ss} (with *ss* labelling classical steady-state solutions)

$$\alpha_{ss} = \frac{\epsilon_a}{\gamma_a - \kappa\beta_{ss}}. \quad (7)$$

We note here that, for $\epsilon_a = 0$, the classical prediction is for a critical threshold value of $\epsilon_b^c = \gamma_a\gamma_b/\kappa$, below which the system does not oscillate. In this case, Eq. (7) is just the normal below threshold solution for optical parametric oscillation, and, with $\epsilon_a \neq 0$, a divergence occurs at the value $\beta_{ss} = \gamma_a/\kappa$. This is exactly the classically predicted above threshold value of β_{ss} without injected signal. Substituting α_{ss} in the equation for β_{ss}, we find a cubic equation for β_{ss},

$$2\kappa^2\gamma_b\beta_{ss}^3 - 2\kappa(2\gamma_a\gamma_b + \kappa\epsilon_b)\beta_{ss}^2 + 2\gamma_a(2\kappa\epsilon_b + \gamma_a\gamma_b)\beta_{ss} - 2\gamma_a^2\epsilon_b + \kappa\epsilon_a^2 = 0. \quad (8)$$

This equation may then be rearranged to give the pump amplitude as a function of the steady-state intracavity field,

$$\epsilon_b = \frac{2\gamma_b\beta_{ss}(\gamma_a - \kappa\beta_{ss})^2 + \kappa\epsilon_a^2}{2(\gamma_a - \kappa\beta_{ss})^2}, \quad (9)$$

which diverges at the threshold value $\beta_{ss} = \gamma_a/\kappa$, indicating that this value cannot be reached in the stationary regime. With $\epsilon_a = 0$, we find the standard below threshold solution, $\beta_{ss} = \epsilon_b/\gamma_b$. We note here that Eq. (9) does not depend on the relative sizes of the pumping terms, and is equally valid for both the OPO and SHG with injected signal, although we must take care with the relative phases of the input fields. We may equally solve for the low-frequency pump, finding

$$\epsilon_a^2 = \frac{2}{\kappa}(\epsilon_b - \gamma_b\beta_{ss})(\gamma_a - \kappa\beta_{ss})^2, \quad (10)$$

which is always positive in SHG ($\epsilon_b = 0$) as β_{ss} is negative for a resonant cavity.

The divergence in Eq. (9) causes a type of potential barrier at the value of the uninjected threshold, with infinite pump power being needed to reach the threshold value of β_{ss}, irrespective of the (finite) size of the injected signal. This is shown in Fig. 1), where we plot the intracavity intensity as a function of the pump power, for values $\gamma_a = \gamma_b = 1$, $\kappa = 10^{-2}$ (which we use throughout this article), and different values of ϵ_a. It is readily seen how the threshold value is approached asymptotically. This feature is not seen in classical predictions without injected signal, where the intracavity field rises monotonically as a function of the pumping until it reaches the threshold value, after which it remains constant, with a discontinuity in the derivative at threshold. The clamping of the high-frequency field at the threshold value without injected signal, irrespective of increasing pumping, is traditionally explained using power conservation [21]. This explanation is still valid, but we have shown that an additional mathematical insight is possible when there is an injected signal present, for which the standard situation of pumping only at the harmonic frequency is a limiting case. In fact, the quantum solutions without injected signal also exhibit a similar be-

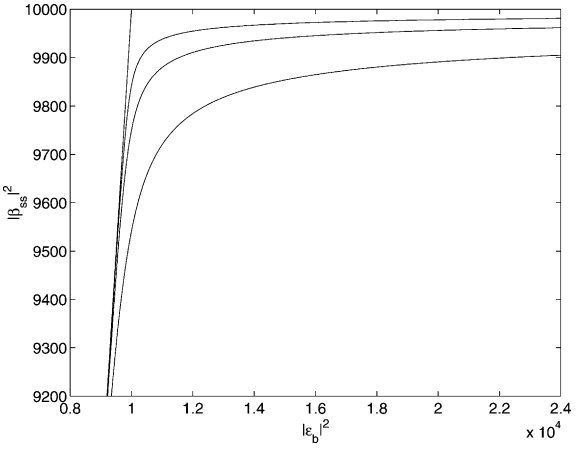

Fig. 1. Classical near threshold solutions for $|\beta_{ss}|^2$ as a function of $|\epsilon_b|^2$ in the degenerate OPO with injected signal, for the parameters $\kappa = 10^{-2}$ and $\gamma_a = \gamma_b = 1$, which are used in all the results shown. The injected signal strength, ϵ_a, varies from 0 (upper curve), through $0.001\epsilon_b^c$, $0.002\epsilon_b^c$ and $0.005\epsilon_b^c$ (lower curve). In this and subsequent graphics, all quantities plotted are dimensionless.

haviour in not reaching the predicted threshold, as has been previously calculated using the complex P-representation [22]. This near threshold behaviour does not have a classical description as without injected signal the conversion begins as a spontaneous process, which needs a quantum description. In the classical analysis, there is no converted field present below threshold. With an injected signal, there is always a macroscopic field at the low frequency, which acts to stimulate the conversion. As the signal strength increases, the stimulated processes become stronger, so that there is no longer a clear threshold for conversion, although as we will show below, there is still a clearly defined critical point.

3.2. Linearised fluctuation analysis

In the OPO we are particularly interested in the quantum properties of the fields in operating regimes where a full quantum analysis is necessary. In order to define these regions, we first linearise Eq. (3) around the classical steady-state solutions. Following the standard procedures [22,23], we then write an evolution equation for the fluctuations. Beginning with Eq. (3), we consider that the variables may be written as the sum of a mean steady-state value and a fluctuation, e.g., $\alpha = \alpha_{ss} + \delta\alpha$, $\alpha^+ = \alpha^*_{ss} + \delta\alpha^+$, etc. To first order in the fluctuations, this gives the following set of equations for $\delta\tilde{x} = [\delta\alpha, \delta\alpha^+, \delta\beta, \delta\beta^+]^T$,

$$\mathrm{d}\delta\tilde{x} = A\delta\tilde{x}\,\mathrm{d}t + B\mathrm{d}W, \tag{11}$$

where $\mathrm{d}W$ is a vector of Wiener increments and

$$B = \begin{bmatrix} \sqrt{\kappa\beta_{ss}} & 0 & 0 & 0 \\ 0 & \sqrt{\kappa\beta^*_{ss}} & 0 & 0 \\ 0 & 0 & 0 & 0 \\ 0 & 0 & 0 & 0 \end{bmatrix}. \tag{12}$$

The drift matrix is found as

$$A = \begin{bmatrix} -\gamma_a & \kappa\beta_{ss} & \kappa\alpha^*_{ss} & 0 \\ \kappa\beta^*_{ss} & -\gamma_a & 0 & \kappa\alpha_{ss} \\ -\kappa\alpha_{ss} & 0 & -\gamma_b & 0 \\ 0 & -\kappa\alpha^*_{ss} & 0 & -\gamma_b \end{bmatrix}. \tag{13}$$

This whole analysis depends on the fact that we can consider the fluctuations as being smaller than the mean values. If the eigenvalues of the drift matrix develop a positive real part, the fluctuations need not remain small, the system becomes unstable and the linearised analysis loses its validity. These eigenvalues have previously been given as functions of the intracavity fields as [20]

$$\begin{aligned} \lambda_{1,2} = & -\frac{1}{2}[-|\kappa\beta_{ss}| + \gamma_a + \gamma_b] \\ & \pm \frac{1}{2}\left[(-|\kappa\beta_{ss}| + \gamma_a - \gamma_b)^2 - 4|\kappa\alpha_{ss}|^2\right]^{1/2}, \\ \lambda_{3,4} = & -\frac{1}{2}[|\kappa\beta_{ss}| + \gamma_a + \gamma_b] \\ & \pm \frac{1}{2}\left[(|\kappa\beta_{ss}| + \gamma_a - \gamma_b)^2 - 4|\kappa\alpha_{ss}|^2\right]^{1/2}. \end{aligned} \tag{14}$$

Without injected signal we have simple expressions for the fields as a function ϵ_b, κ and $\gamma_{a,b}$ both above and below threshold. With injected signal, the solutions required are those of the cubic equation for β_{ss} Eq. (8) and the expression for α_{ss} Eq. (7), which become rather messy and are not particularly enlightening. Hence in this case it is easier to proceed numerically, but we will first define regions where different behaviours may be expected in a classical analysis.

It has previously been found that there are several instabilities present in the system when it is pumped at both frequencies, with a phase diagram having been developed [20] from an analysis of the steady-state solutions. We have reproduced this phase diagram for different parameters in Fig. 2 and will investigate the behaviour in different regions in Section 4. In this figure, there are four main regions, with the boundaries being found by analysing the solutions of a cubic equation for real α_{ss},

$$\alpha^3_{ss} + \left(\frac{2\gamma_a\gamma_b}{\kappa^2} - \frac{2\epsilon_b}{\kappa}\right)\alpha_{ss} - \frac{2\gamma_b\epsilon_a}{\kappa^2} = 0. \tag{15}$$

Analysing the roots of this equation using Cardano's formula [24] shows that the relation

$$\epsilon_b = \epsilon^c_b + \frac{3}{2}\kappa^2\left(\frac{\gamma_b\epsilon_a}{\kappa^2}\right)^{2/3} \tag{16}$$

defines the boundaries between regions where only one real solution exists and where there are three. In our figure, these are the lines dividing region 2 from regions 3 and 4. For the pump and signal in

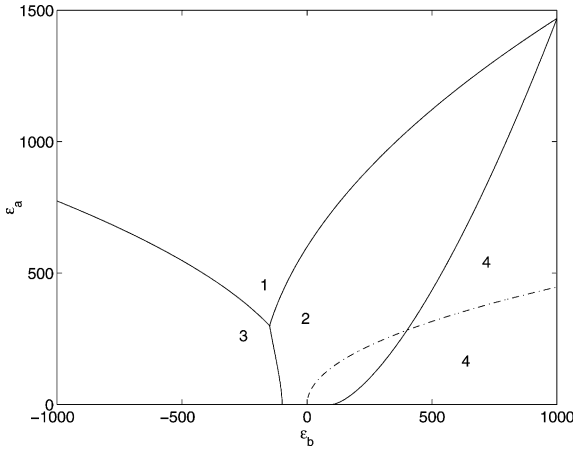

Fig. 2. Phase diagram for the real solutions of sub/second harmonic generation in the steady state. Region 1 contains self-pulsing solutions, region 2 contains single-valued solutions, while regions 3 and 4 contain three solutions.

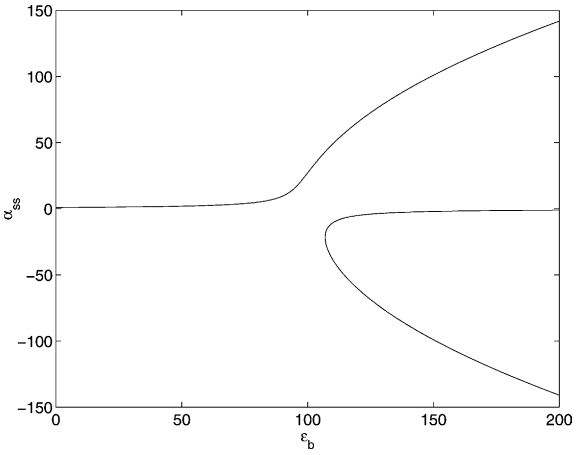

Fig. 3. Classical solutions for α_{ss} as a function of ϵ_b in the degenerate OPO with injected signal, for the parameters $\kappa = 10^{-2}$ and $\gamma_a = \gamma_b = 1$ and $\epsilon_a = 0.01\epsilon_b^c$. The multiple solutions are readily seen, as is the shifting of the threshold for this to a pump power higher than $\epsilon_b^c = 100$ without injected signal. The lower branch is unstable.

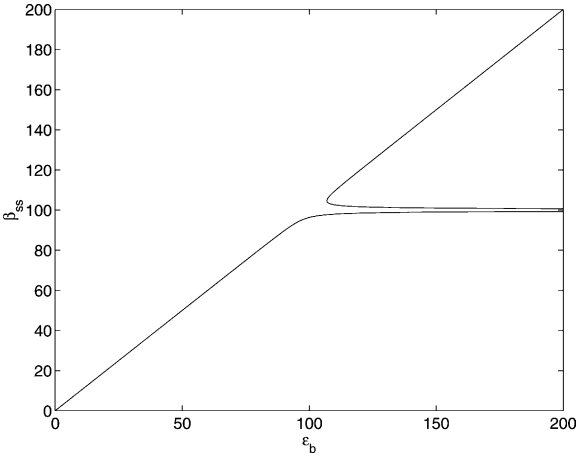

Fig. 4. Classical solutions for β_{ss} as a function of ϵ_b in the degenerate OPO with injected signal, for the same parameters as Fig. 3. The upper branch is unstable.

phase, it is in region 4 that we find multi-valued solutions. In this region, there are always eigenvalues of the matrix A with a positive real part, so that a linearised fluctuation analysis may not be valid. For the signal out of phase with the (positive) pump, these solutions are found in region 3. In region 2 there exists only one real solution, while region 1 exhibits hard mode oscillations and is where self-pulsing behaviour is found. The dash-dotted line defines a boundary below which downconversion may be thought of as the dominant process and above which second harmonic generation dominates, as will be described in more detail in Section 4.3. At the intersection of regions 1, 2 and 3, three different behaviours are possible, which will be investigated below, as a linearised analysis is not valid here. In fact, a numerical analysis of the eigenvalues shows that it is only in region 2 that we may expect a linearised analysis to be fully valid, with unstable solutions always being present in the other regions.

In Figs. 3 and 4, we show the classical steady-state solutions for the amplitudes as a function of the high-frequency pump, for parameters $\gamma_a = \gamma_b = 1$, $\kappa = 10^{-2}$ and $\epsilon_a = 0.01\epsilon_b^c$. Without injected signal, $\epsilon_b^c = 100$ for the parameters we use in this article. Looking at Fig. 3, we see that above a certain pumping value, there are three possible solutions, while below this there is only one. The point at which the three solutions develop is also the point at which the drift matrix of the fluctuations can develop positive real parts of the eigenvalues, and is shifted above the value of critical pumping for pure downconversion. This is exactly the region defined by the division between regions

2 and 4 in Fig. 2. In Fig. 4, the stable steady-state solutions follow the lower line, not entering into the upper, unstable solutions.

The region of multi-valued solutions occurs when there are three real solutions for the cubic equation obtained for α_{ss} [20]. Without injected signal, it manifests itself as the two well-known above threshold solutions, $\alpha_{ss} = \pm\sqrt{2(\epsilon_b - \epsilon_b^c)/\kappa}$, and a solution $\alpha_{ss} = 0$, which is unstable. With injected signal, we consider the case where ϵ_a is positive and, by rearranging Eq. (16), we find the condition

$$\left(\frac{\gamma_b\epsilon_a}{\kappa^2}\right)^2 + \frac{8}{27}\left(\frac{\gamma_a\gamma_b}{\kappa^2} - \frac{\epsilon_b}{\kappa}\right)^3 < 0. \tag{17}$$

Writing $\epsilon_b = m\epsilon_b^c$, where $m > 1$, we find three real solutions for

$$\epsilon_a < \sqrt{\frac{8\gamma_a^3\gamma_b}{27\kappa^2}(m-1)^3}. \tag{18}$$

As an example, for the parameters we use below ($\kappa = 0.01$ and $\gamma_a = \gamma_b = 1$), with $m = 1.1$, this gives a maximum value of $\epsilon_a \approx 0.017\epsilon_b^c$ for the existence of the three real solutions.

3.3. Full quantum analysis

To perform a fully quantum analysis of this system, we revert to numerical stochastic integration of Eq. (3), particularly in the regions where a semiclassical analysis is not expected to be valid. Without injected signal, it has been calculated that the maximum of noise compression occurs slightly above the threshold pumping value [25]. We, therefore, focussed our attention on this region. The time development of the intracavity intensities and Y quadrature variances are shown in Figs. 5 and 6, for $\epsilon_b = 1.1\epsilon_b^c$ and differing values of the injected signal. (Note that we define the quadratures as $X_a = \hat{a} + \hat{a}^\dagger$ and $Y_a = -\mathrm{i}(\hat{a} - \hat{a}^\dagger)$, so that variances in a coherent state are equal to 1.) The lines (a, b, c) are the result of the averaging of 3.8×10^4, 1.03×10^5 and 8.3×10^5 stochastic trajectories of the positive-P representation equations, respectively. What we see in both graphs is that, as the injected signal is increased, the steady-state values are attained more rapidly. This is representative of a critical slowing down [23] and

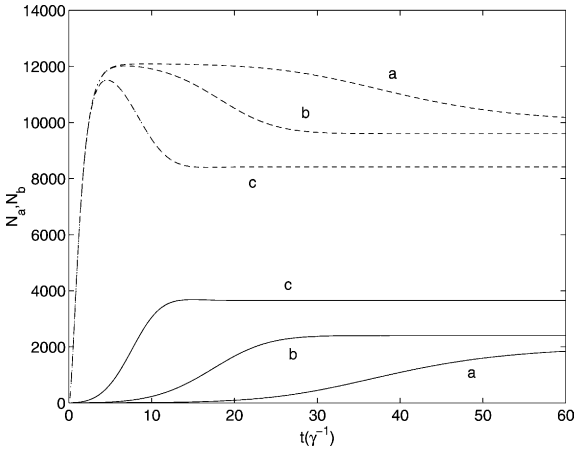

Fig. 5. Quantum solutions for the intracavity intensities in the degenerate OPO with injected signal, for $\gamma_a = \gamma_b = 1$, $\kappa = 0.01$ and $\epsilon_b = 1.1\epsilon_b^c$. The solid lines are for $N_a(= \overline{\alpha^+\alpha})$, with the dashed lines representing $N_b(= \overline{\beta^+\beta})$. The values of ϵ_a are (a) 0, (b) $0.01\epsilon_b^c$ and (c) $0.05\epsilon_b^c$. While (b) and (c) reach the steady-state over this time scale, (a) is still in the transient regime.

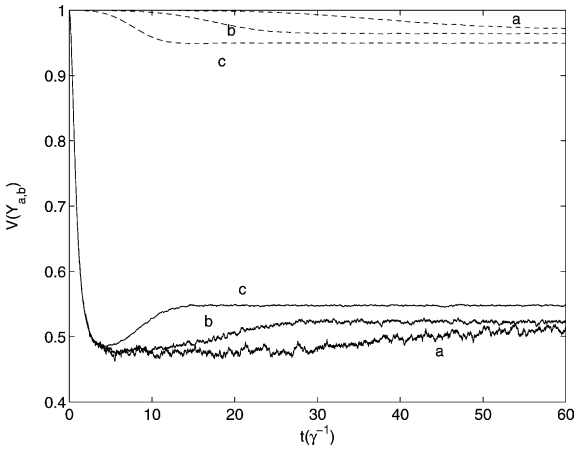

Fig. 6. The Y quadrature variances for the two intracavity fields, for the same parameters as in Fig. 5. The solid lines are $V(Y_a)$ and the dash-dotted lines are $V(Y_b)$. The irregularity of the two lower lines is due to the finite number of trajectories sampled.

indicates that the injected signal moves the system away from criticality by moving the onset of positive eigenvalues of the fluctuation drift matrix to a higher pump power. It is the onset of these positive eigenvalues that mathematically defines the onset of critical instabilities in the system. The

further the system is from the onset of positive eigenvalues, the quicker the transients disappear and it relaxes to its stationary state. We also see in Fig. 6 that, as the injected signal is increased, there is less squeezing in the fundamental and more in the harmonic. The results for (a) and (b) are from region 4 of Fig. 2, while (c) is from just outside this region.

What we also noticed is that, a little above the normal threshold, the variance of the X_a quadrature decreases with injected signal, while the variance of the Y_a quadrature remains almost unchanged. This can be explained by the fact that, without injected signal, there are two possible physical branches for α_{ss}, with opposite phase. The variance in X_a is then approximately equal to $\langle X_a^2 \rangle$, as $\langle X_a \rangle$ is zero. With in-phase injected signal, the stochastic integration begins to prefer the upper branch, with the multi-valuedness in α_{ss} being removed as a phase reference is provided for the physical solution. The branch with the same sign as the signal begins to dominate, with $\langle X_a \rangle$ becoming non-zero. With a sufficiently strong signal, it is only the local distribution around the populated branch which contributes to the variance, which then becomes much smaller. As an example, the results of the stochastic integration show that, in the steady-state, for $\epsilon_b = 1.1\epsilon_b^c$, without injected signal, $V(X_a) \approx 8000$ and $\langle X_a \rangle = 0$, with the stable classical solutions $2\alpha_{ss} = \pm 89.4$. (For a real field, $\langle X_a \rangle = 2\alpha_{ss}$.) When we inject a signal, $\epsilon_a = 0.01\epsilon_b^c$, we find $V(X_a) \approx 5.5$ and $\langle X_a \rangle \approx 98$. In both these cases, $V(Y_a) \approx 0.5$ and $\langle Y_a \rangle = 0$. The injection of the signal serves to increase the intensity of the intracavity field at the fundamental, while at the same time moving it much closer to being in a minimum uncertainty state, without degrading the squeezing in the Y_a quadrature. Such a source of bright squeezed light may prove useful for possible applications.

4. Sub-second harmonic generation

In Fig. 2, we see various operating regimes, ranging from pure downconversion on the ϵ_b axis to pure second harmonic generation on the vertical line $\epsilon_b = 0$. As is well known, in SHG with real pumping, it is the X_a quadrature which exhibits squeezing in the fundamental, while in the OPO it is the Y_a quadrature. In second harmonic generation, ($\epsilon_a \gg \epsilon_b$) the amplitude of the fundamental is given by Eq. (7), which will not exhibit threshold behaviour as β_{ss} is negative for a resonant cavity with a positive pump. Combined with Eq. (10), we see that there will be no divergences in the pumping, with both field intensities increasing with increasing pump power. In contrast to below threshold optical parametric oscillation, which is a spontaneous process, we do not expect that the injection of a signal field would markedly increase the efficiency of the conversion in SHG. This is because downconversion depends on the existence of fluctuations as a trigger, while SHG does not, being able to proceed in a fully classical description without any noise in the fields. Of course, such a description would not be able to describe the resulting quantum features of the fields produced. We will concentrate below on three main aspects of the behaviour. The first is the change in the fields with small changes in the parameters at and near the triple point of the phase diagram. The second is that the injection of a signal field does change the behaviour of the steady-state fields in the self-pulsing regime [26,27]. The third feature, perhaps less expected, is that rather than enhance conversion, certain values of signal can actually stop the generation of the second harmonic altogether.

4.1. Near the triple point

We will now investigate the quantum properties of the fields near the triple point shown in Fig. 2. What is interesting in this region is that, with small changes in the pumping fields, we can move between three different operational regimes, two of which possess unstable solutions, in a manner resembling a phase transition. For the parameters used for stochastic integration in this article, $\kappa = 10^{-2}$ and $\gamma_a = \gamma_b = 1$, the triple point lies at $(\epsilon_b^t = -150, \epsilon_a^t = 300)$. We will not present semi-classical results here, as the drift matrix for the fluctuations always has negative real parts to the eigenvalues in regions 1 and 3 in the vicinity of the triple point, hence we do not expect linearised results to be reliable.

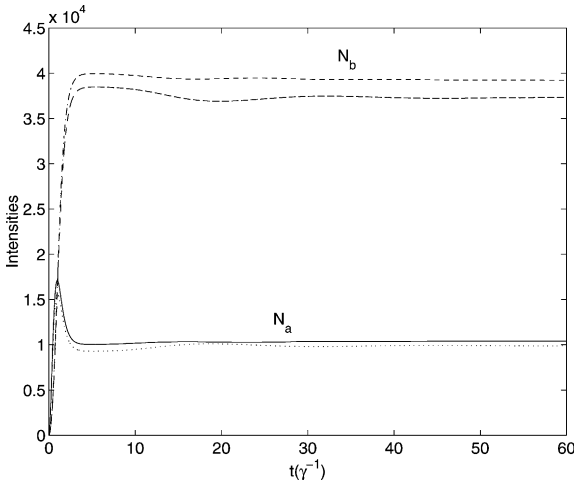

Fig. 7. Behaviour of the mean fields at and near the triple point of Fig. 2. The behaviour in region 1 is quantitatively similar to that at the triple point, shown as the upper lines for both $N_a(=\overline{\alpha^+\alpha})$ and $N_b(=\overline{\beta^+\beta})$. The behaviour in region 3 is very similar to that in region 2, shown as the lower lines.

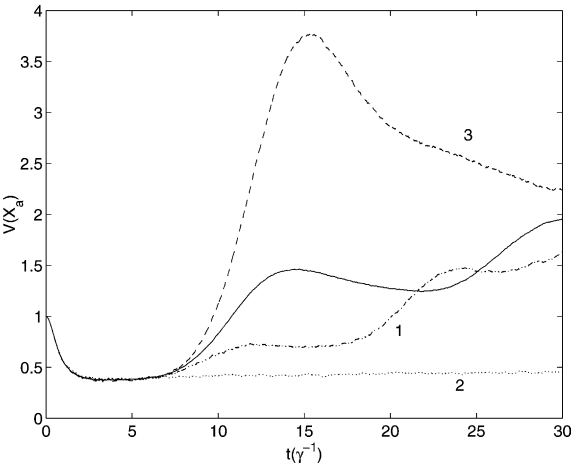

Fig. 8. Short time behaviour of the X_a quadrature variances at and near the triple point. The X_b variance only shows a small amount of transient squeezing for all the parameter regions considered. The solid line is for the triple point, with the other lines being numbered by region.

In Fig. 7 we show the short-time development of the intracavity fields. The upper lines for each field were calculated right at the triple point, using 1.13×10^5 stochastic trajectories of Eq. (3). Over the time shown, the solutions for the intensities in region 1, with $\epsilon_a = 1.05\epsilon_a^{\mathrm{t}}$ and $\epsilon_b = \epsilon_b^{\mathrm{t}}$, averaged over 1.95×10^4 trajectories, were qualitatively similar to those at the triple point. The lower lines represent the solutions for region 2, using 2.1×10^4 trajectories, for $\epsilon_a = 0.97\epsilon_a^{\mathrm{t}}$ and $\epsilon_b = 0.95\epsilon_b^{\mathrm{t}}$. Solutions obtained for region 3, with 1.5×10^4 trajectories and for $\epsilon_a = 0.95\epsilon_a^{\mathrm{t}}$ and $\epsilon_b = \epsilon_b^{\mathrm{t}}$, are again qualitatively similar. What is not readily apparent from this graph is that it is only the solution for region 2 that has entered the steady-state regime over this time scale. The solutions in region 1, in the self-pulsing regime of the phase space, continued to increase slowly up to at least a time of $140\gamma^{-1}$, although self-pulsing behaviour was not seen before this time. It is possible that there would be a signature of this behaviour in frequency space, as was found for SHG with an added $\chi^{(3)}$ non-linearity, appearing before evidence was visible in the time domain [13]. Note that in these solutions, $|\beta_{\mathrm{ss}}|^2$ would be in violation of the threshold value found using Eq. (9) if β_{ss} were positive.

The lack of stationarity is evident in Fig. 8, which shows the X quadrature variances for the same parameters as in Fig. 7. What is immediately obvious is that, although all regimes exhibit a small amount of transient squeezing as the cavity begins to be pumped, this is only persistent in region 2, the region of real solutions. The variances at the triple point (solid line) and for region 1 continue to grow, while that for region 3 has begun to relax toward its steady-state value over the time shown. In fact, in the region near the triple point, both fields are far from being in minimum uncertainty states for the parameters we have considered. Considering also the Fano factors (defined as the normally ordered intensity variance divided by the expectation value of the intensity), we see that the closest is the fundamental in region 2, which exhibits a steady-state Fano factor of approximately 1, and an X_a quadrature variance of approximately 0.45, but a Y_a quadrature variance of approximately 310. The noisiest fields are found in region 1, with Fano factors of approximately 40 in both harmonic and fundamental at $t = 140\gamma^{-1}$, a variance in X_a of approximately 8, and a variance in Y_a of almost 5000. This demonstrates just how the properties of the fields can be extremely sensitive to perturbations near critical operating

points, with huge changes being found in the quantum statistics of the fields due to relatively minor changes in the input fields.

4.2. Self-pulsing regime

Without an injected signal, it is well known that a Hopf bifurcation exists at a critical pumping strength [26,27], $\epsilon_a^{sp} = (1/\kappa)(\gamma_a+2\gamma_b)\sqrt{2\gamma_b(\gamma_a+\gamma_b)}$. For higher pump powers, both fields exhibit limit cycle behaviour, with the steady state being one of periodic oscillations. With pumping at both frequencies, this behaviour is found in region 1 of Fig. 2. With pure SHG it happens on a vertical line beginning at the point $(\epsilon_b = 0, \epsilon_a = 600)$. It is obvious from the phase diagram that the addition of a non-zero ϵ_b can modify the self-pulsing behaviour. As can be seen from the phase diagram, a negative injected signal can actually allow self-pulsing for a lower pump power, at least until the triple point is reached. On the other hand, a positive injected signal always means that a higher pump power is needed to enter the self-pulsing regime. It is then natural to expect that any injected signal will change the properties of the fields in this region.

In Fig. 9, we show the results of stochastic integration for $\epsilon_a = 2\epsilon_a^{sp}$, with and without an injected signal. The results shown are an average of 10^4 stochastic trajectories. The injected signal strength used was $0.15\epsilon_a^{sp}$, and had a small, but experimentally detectable effect on the oscillatory behaviour of the fundamental. The effect on the harmonic intensity is especially marked and should be easily detectable. Looking at Fig. 2, both these parameter regimes are found well within the self-pulsing area of the graph, at the points $(\epsilon_b = 0, \epsilon_a = 1200)$ and $(\epsilon_b = 90, \epsilon_a = 1200)$, respectively. We note here that the stochastic integration with this strength of injected signal was noticeably less stable than without, developing spiked behaviour at a little more than the maximum time shown in Fig. 9. This is not likely to be the result of a bad integration algorithm, but indicates that the positive-P distribution may have begun to develop a power law tail, so that the boundary terms could no longer be neglected [28]. This is a well-known problem with the positive-P

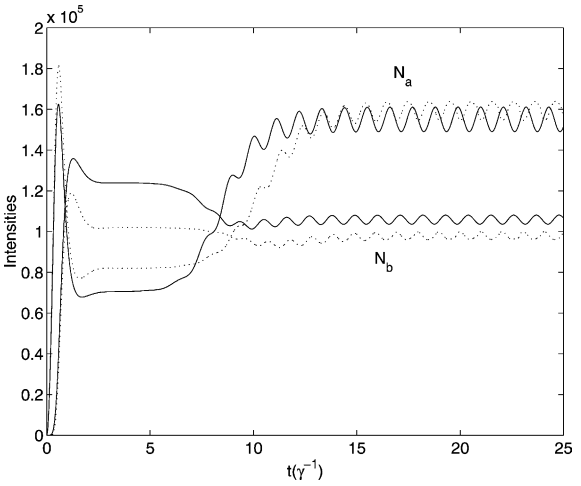

Fig. 9. Changes to the self-pulsing behaviour in second harmonic generation due to the injection of a signal field. The pump is at twice the self-pulsing threshold, $\epsilon_a = 2\epsilon_a^{sp}$, and the injected signal strength used was $0.15\epsilon_a^{sp}$. $N_a(=\overline{\alpha^+\alpha})$ and $N_b(=\overline{\beta^+\beta})$.

representation and solutions have been proposed [29,30], but a detailed analysis is outside the scope of this article. Interestingly enough, as ϵ_b was increased further so that the parameter regime moved towards the boundary of regions 1 and 2 of Fig. 2, the integration eventually became stable again. Near the boundary and in region 2, where the injected signal caused the self-pulsing oscillations to disappear, the integration is completely stable up to at least $t = 200\gamma^{-1}$, the maximum that we were able to investigate.

4.3. Blocking of the harmonic via injected signal

An interesting property of second harmonic generation with injected signal is that, under certain circumstances, an injected signal at the second harmonic can actually act to stop conversion altogether and can also change the quadrature which exhibits noise-suppression. In the case where the cavity losses at the high-frequency mode are much higher than those of the low-frequency mode, it has previously been predicted that, for the critical value of pumping, an injected signal could change the squeezed quadrature [31]. Here, we show that this behaviour also exists in a more general sense,

over a range of pump values and loss rates. Examining Eq. (8), we see that for the relative pumping strengths $\epsilon_b^V = \kappa\epsilon_a^2/2\gamma_a^2$, (shown as the dash-dotted line in Fig. 2) one possible solution is $\beta_{ss} = 0$ and we are left with the quadratic equation

$$\kappa^2\gamma_b\beta_{ss}^2 - \kappa(2\gamma_a\gamma_b + \kappa\epsilon_b)\beta_{ss} + \gamma_a(2\kappa\epsilon_b + \gamma_a\gamma_b) = 0. \tag{19}$$

In this case the other two solutions are

$$\beta_{ss} = \frac{2\gamma_a\gamma_b + \kappa\epsilon_b}{2\kappa\gamma_b} \pm \sqrt{\frac{\epsilon_b(\kappa\epsilon_b - 4\gamma_a\gamma_b)}{4\kappa\gamma_b^2}}, \tag{20}$$

which are complex in region 2 of Fig. 2 and hence will not manifest themselves. In region 4, with $\epsilon_b > 4\gamma_a\gamma_b$, there are three real solutions, but only the zero solution is stable. The point $(\epsilon_b = 4\gamma_a\gamma_b/\kappa, \epsilon_a = 2\gamma_a\sqrt{2\gamma_a\gamma_b}/\kappa)$ in the phase diagram, which is the intersection of the dash-dotted line with the boundary between regions 2 and 4, marks the transition from one to three real solutions.

Stochastic integration over a wide range of parameters always chooses the zero solution for β_{ss}, as expected. The stable solution is that with no intracavity field at the harmonic frequency and the same field that would exist without the crystal at the fundamental, or $\alpha_{ss} = \epsilon_a/\gamma_a$. The results show that it is indeed as if the crystal is not present as far as the fundamental is concerned, with the statistics of both fields being those of coherent states. In the case of the harmonic, this is a coherent vacuum. A linearised fluctuation analysis in this region indeed shows that the steady-state spectra are those of the input fields, with the diffusion matrix being null. A comparison between the intracavity fields with and without injected signal is shown in Fig. 10, obtained via stochastic integration of 2.5×10^4 trajectories of the positive-P equations, showing that the steady-state harmonic is indeed vacuum. It is as if the signal field has turned the crystal transparent to the pump at the fundamental frequency. What happens mathematically in the classical description is that β_{ss} changes from negative below the dash-dotted line to positive above it. As the process is continuous, it must pass through zero for a particular value of ϵ_b.

The dash-dotted line $\epsilon_a = \gamma_a\sqrt{2\epsilon_b/\kappa}$ in Fig. 2 also defines the division of the regions where

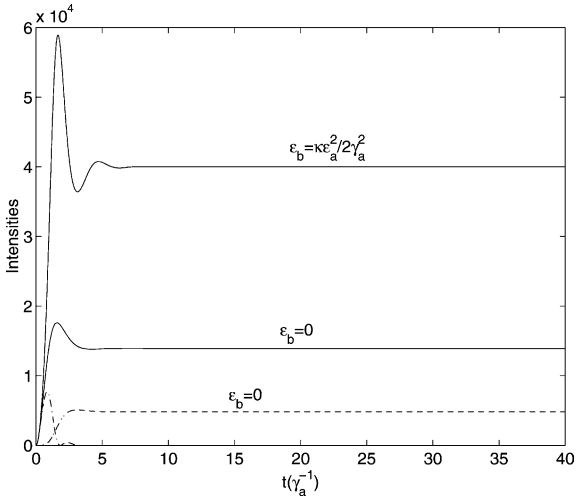

Fig. 10. Results of stochastic integration showing the disappearance of the steady-state second harmonic due to the injection of a signal field, $\epsilon_b = \kappa\epsilon_a^2/2\gamma_a^2$. The solid lines represent the fundamental, $N_a(=\overline{\alpha^+\alpha})$, and the dash-dotted lines the second harmonic, $N_b(=\overline{\beta^+\beta})$, for $\epsilon_a = 200$. With injection, the harmonic disappears after a brief transient.

squeezing is found in the X quadratures (above) and where it is found in the Y quadratures (below), as well as the change of sign of β_{ss}, which is positive below the line and negative above it. As these different squeezing characteristics are typical of second harmonic generation and downconversion, respectively, this line can be thought of as defining the a division between a region where second harmonic generation is predominant and a region where downconversion is predominant. In region 2, a linearised analysis is valid, allowing for a particularly simple calculation of the spectra via the formula

$$S(\omega) = (A + \mathrm{i}\omega)^{-1}BB^{\mathrm{T}}(A^{\mathrm{T}} - \mathrm{i}\omega)^{-1}, \tag{21}$$

where A and B are from Eq. (11). The output spectra for the low-frequency mode are easily found by multiplying the sum of the appropriate matrix elements by $2\gamma_a$ and adding one because of the normal ordering. We show the resulting output quadrature spectra in Figs. 11 and 12, demonstrating how the squeezing in the X_a quadrature decreases as the injected signal strength increases, until it vanishes at the value ϵ_b^V and then begins to exhibit excess noise. The Y_a quadrature exhibits the

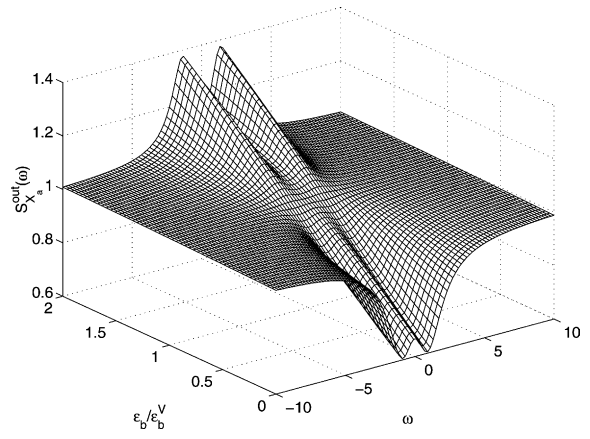

Fig. 11. The output spectrum of the X_a quadrature as the system changes from second harmonic generation to downconversion due to the injected signal field, with $\epsilon_a = 100$. ϵ_b is normalised to the value $\epsilon_b^V = .5\kappa\epsilon_a^2/\gamma_a^2$.

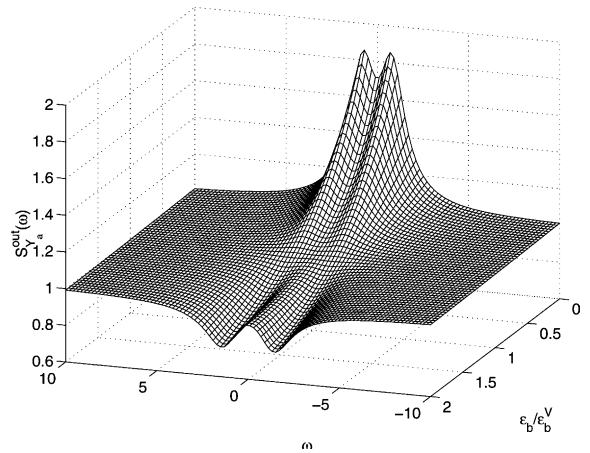

Fig. 12. The output spectrum of the Y_a quadrature as the system changes from second harmonic generation to downconversion due to the injected signal field, with $\epsilon_a = 100$. ϵ_b is normalised to the value $\epsilon_b^V = .5\kappa\epsilon_a^2/\gamma_a^2$.

opposite behaviour, being antisqueezed below ϵ_b^V and squeezed above this value. It is possible that this behaviour could have some use as a switching device, or to provide tunable squeezing.

5. Conclusions

We have investigated the intracavity parametric processes of second harmonic generation and degenerate downconversion, both with injected coherent signal fields, describing a rich variety of different behaviours. The addition of an injected signal changes the well-known threshold behaviour in the optical parametric oscillator, in a way which gives further physical insight into the uninjected behaviour. Above the standard threshold, signal injection serves to bring the field at the fundamental closer to a minimum uncertainty state while at the same time preserving the squeezing in the Y_a quadrature. As the injection also increases the intensity, we find a more intense field than in the uninjected case. This may well have applications in spectroscopy, for example. Near the triple point where different operating regions meet, the behaviour of the fields shows a sensitive dependence on initial conditions, with small changes in the input fields able to produce drastic changes in the intracavity fields, especially in the quantum statistics. In the self-pulsing regime of second harmonic generation, an injected field at the harmonic frequency is shown to effect the self-pulsing behaviour. We also find that an injected signal of the appropriate strength at the harmonic can actually stop the process of second harmonic generation, with the cavity seeming to be empty as far as the fundamental is concerned. This behaviour occurs on the boundary between downconversion and second harmonic generation and could possibly be used, with variable injection, to switch squeezing between quadratures, as well as to change the phase of the harmonic.

Acknowledgements

This research was supported by the New Zealand Foundation for Research, Science and Technology (UFRJ0001), the Brazilian agency CNPq (Conselho Nacional de Desenvolvimento Científico e Tecnológico) and the Deutsche Forschungsgemeinschaft under contract FL210/11.

References

[1] M. Martinelli, C.L.G. Alzar, P.H.S. Ribeiro, P. Nussenzveig, Braz. J. Phys. 31 (2001) 597.

[2] R. Andrews, E.R. Pike, S. Sarkar, Opt. Exp. 10 (2002) 461.
[3] Y.J. Lu, Z.Y. Ou, Phys. Rev. A 62 (2000) 033804.
[4] R. Zambrini, S.M. Barnett, P. Colet, M. San Miguel, Phys. Rev. A 65 (2002) 023813.
[5] C. Lamprecht, M.K. Olsen, M.J. Collett, H. Ritsch, Phys. Rev. A 64 (2001) 033811.
[6] K.S. Zhang, T. Coudreau, M. Martinelli, A. Maître, C. Fabre, Phys. Rev. A 64 (2001) 033815.
[7] A. Porzio, A. Chiummo, F. Sciarrino, S. Solimento, Optics and Lasers in Engineering 37 (2002) 585.
[8] See, for example,P. Meystre, D.F. Walls (Eds.), Nonclassical Effects in Quantum Optics, A.I.P., New York, 1991.
[9] M. Bache, P. Scotto, R. Zambrini, M. San Miguel, M. Saffman, Phys. Rev. A 66 (2002) 013809.
[10] M.A.M. Marte, Phys. Rev. A 49 (1994) 3166.
[11] M.A.M. Marte, Phys. Rev. Lett. 74 (1995) 4815.
[12] A.G. White, P.K. Lam, M.S. Taubman, M.A.M. Marte, S. Schiller, D.E. McClelland, H.A. Bachor, Phys. Rev. A 55 (1997) 4511.
[13] M.K. Olsen, V.I. Kruglov, M.J. Collett, Phys. Rev. A 63 (2001) 033801.
[14] M.K. Olsen, S.C.G. Granja, R.J. Horowicz, Opt. Commun. 165 (1999) 293.
[15] I.E. Protsenko, L.A. Lugiato, C. Fabre, Phys. Rev. A 50 (1994) 1627.
[16] M.J. Collett, D.F. Walls, Phys. Rev. A 32 (1985) 2887.
[17] P.D. Drummond, C.W. Gardiner, J. Phys. A 13 (1980) 2353.
[18] C.W. Gardiner, Quantum Noise, Springer, Berlin, 1991.
[19] P.D. Drummond, K.J. McNeil, D.F. Walls, Opt. Acta 28 (1981) 211.
[20] P.D. Drummond, K.J. McNeil, D.F. Walls, Opt. Acta 27 (1980) 321.
[21] A. Yariv, Quantum Electronics, Wiley, New York, 1989.
[22] D.F. Walls, G.J. Milburn, Quantum Optics, Springer, Berlin, 1995.
[23] C.W. Gardiner, Handbook of Stochastic Methods, Springer, Berlin, 1985.
[24] M. Abramowitz, I.A. Stegun, Handbook of Mathematical Functions, Dover, New York, 1972.
[25] P.D. Drummond, K. Dechoum, S. Chaturvedi, Phys. Rev. A 65 (2002) 033806.
[26] H. Haken, H. Ohno, Opt. Commun. 16 (1976) 205.
[27] K.J. McNeil, P.D. Drummond, D.F. Walls, Opt. Commun. 27 (1978) 292.
[28] A. Gilchrist, C.W. Gardiner, P.D. Drummond, Phys. Rev. A 55 (1997) 3014.
[29] L.I. Plimak, M.K. Olsen, M.J. Collett, Phys. Rev. A 64 (2001) 025801.
[30] P. Deuar, P.D. Drummond, Phys. Rev. A 66 (2002) 033812.
[31] G.J. Milburn, D.F. Walls, Phys. Rev. A 27 (1983) 392.